Volume 12
Number 25
7 July 2020
Pages 13167-13842

Nanoscale

rsc.li/nanoscale

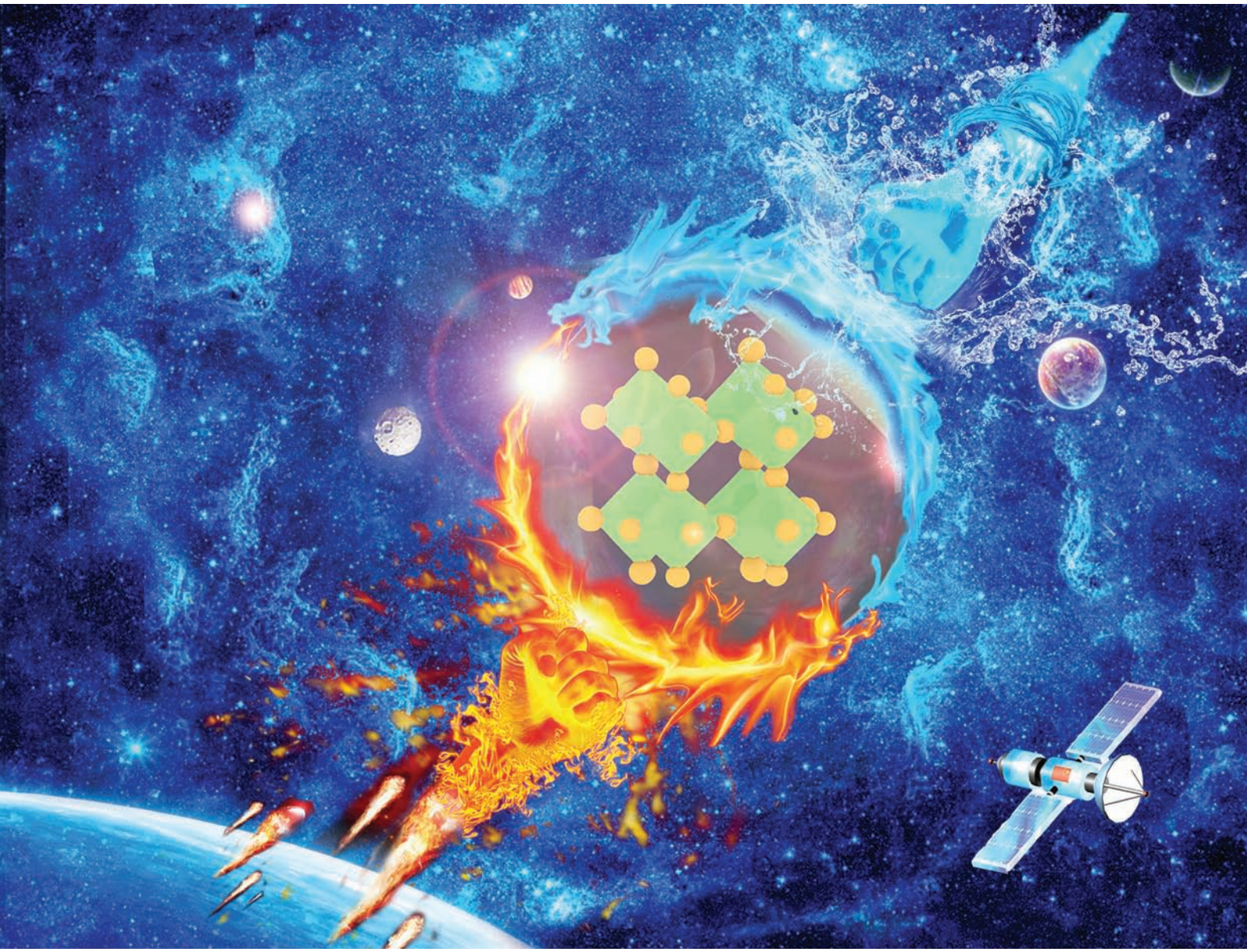

ISSN 2040-3372

ROYAL SOCIETY OF CHEMISTRY

PAPER
Xuyong Yang, Zhipeng Wei, Rui Chen *et al.*
Surface modification of all-inorganic halide perovskite nanorods by a microscale hydrophobic zeolite for stable and sensitive laser humidity sensing

NCNST

Nanoscale

ROYAL SOCIETY OF CHEMISTRY

PAPER

Cite this: *Nanoscale*, 2020, **12**, 13360

Surface modification of all-inorganic halide perovskite nanorods by a microscale hydrophobic zeolite for stable and sensitive laser humidity sensing†

Ruxue Li,[a,b,c] Jiahao Yu,[a] Sheng Wang,[d] Yueqing Shi,[a] Zhaojin Wang,[a] Kai Wang,[a] Zhenhua Ni,[b] Xuyong Yang, *[d] Zhipeng Wei*[c] and Rui Chen *[a]

Received 6th March 2020,
Accepted 7th May 2020

DOI: 10.1039/d0nr01889a

rsc.li/nanoscale

Perovskite materials are very sensitive to the environment which is beneficial for humidity sensing. However, the existing illuminating humidity sensor has low luminous efficiency and sensitivity. Besides, the stability of perovskite materials remains a key issue to be resolved. Compared to luminescence, lasing is much more sensitive to the surrounding environmental situation. However, humidity sensing based on perovskite lasing has not been reported so far. In this work, all-inorganic halide perovskite $CsPbBr_3$ nanorods with an optical gain coefficient as high as 954 cm^{-1} were designed and fabricated. Moreover, a microscale hydrophobic zeolite was introduced to modify perovskites for improved stability. It is interesting to note that the hydrophobic zeolite introduces strong scattering which is beneficial for three-dimensional random lasing with a quality (Q) factor of 2263. Through the strategy of using lasing instead of luminescence, optical stability and sensitive laser humidity sensing were demonstrated, and it exhibits high sensitivity and good reliability. This work provides a new idea of improved stability of perovskites, which will promote the practical application of perovskite materials and devices.

Introduction

Lead halide perovskites $APbX_3$ (A = CH_3NH_3 (MA), Cs, $CH(NH)_2$, (FA); X = Cl, Br, I) possess unique properties such as long balanced electron–hole diffusion length, large absorption coefficient, high carrier mobility, and low defect density, which have been intensively investigated for photovoltaic and optoelectronic devices.[1,2] With the rapid increase of solar cell efficiency (from 3.8 to 24.02%),[3,4] over the past few years, other perovskite-based optoelectronic devices have also been explored, for example, photodetectors,[5] light-emitting diodes (LEDs),[6] and lasers.[6–8] In recent years, perovskites have also been designed for sensing because of their environmental sensitivity, such as the detection of temperature,[9] humidity,[10] gases,[11] metal ions and explosive species.[12,13] Among them, the humidity sensing of perovskites is the most studied by researchers.

In some specific cases, water will cause serious disasters such as explosions and fires in certain chemical processes.[14,15] Until now, perovskite humidity sensing in an optical or electrical manner has been reported.[10,16] The luminescence method has the advantages of high sensitivity and rapid responsivity, and has been considered as a reliable and powerful approach.[17,18] However, in most of the cases, those organic luminescent humidity sensors generally have weak luminescence and low sensitivity. Even for $CH_3NH_3PbBr_3$ with excellent optical properties, the sensitivity is still poor in relative humidity (RH) above 50%.[10,19] However, it is needed to mention that besides a wide range of sensing, a narrow range of sensing sometimes is required in special applications, such as the working environment under high humidity. It is worth noting that for humans, a small change of humidity in low RH does not cause discomfort. However, if the environmental RH is higher than 70%, it will cause our body to secrete excessive pineal hormone, which makes people listless and easily suffer from arthralgia syndrome.[20]

In addition to enhance the sensitivity of perovskite sensing, the stability of perovskite materials remains a key issue to be

[a]*Department of Electrical and Electronic Engineering, Southern University of Science and Technology, Shenzhen, Guangdong 518055, P. R. China. E-mail: chenr@sustech.edu.cn*
[b]*School of Physics, Southeast University, Nanjing, Jiangsu 211189, P. R. China*
[c]*State Key Laboratory of High Power Semiconductor Lasers, Changchun University of Science and Technology, School of Science, Changchun, Jilin 130022, P. R. China. E-mail: zpweicust@126.com*
[d]*Key Laboratory of Advanced Display and System Applications of Ministry of Education, Shanghai University, Shanghai 200072, P. R. China. E-mail: yangxy@shu.edu.cn*

†Electronic supplementary information (ESI) available. See DOI: 10.1039/d0nr01889a

resolved.[6,8,10] For example, it has been shown that compared with traditional materials,[21] the structural phase transitions of perovskite materials seriously influence their optoelectronic device performance.[22,23] Besides, at high temperatures, perovskite materials show significant weight loss due to thermal decomposition.[24] Furthermore, the environmental instability of unmodified perovskites has also been reported.[25] Many strategies have been proposed to solve the problems, such as encapsulating perovskites with organic or inorganic materials.[25,26] However, the surface coating of thick shells will influence the luminescent performance. Moreover, the perovskite nanomaterials also need good dispersion in order to achieve high optical performance.[27] The crystal doping may increase the formation energy of perovskites, but it was still affected by humidity.[28] Therefore, reliable perovskite humidity sensing with high stability and sensitivity is urgent and critical, especially for high RH.

Compared to luminescence, lasing is much more sensitive to the surrounding environmental conditions. However, to the best of our knowledge, humidity sensing based on perovskite lasing has not been reported. To achieve this goal, two requirements need to be fulfilled. First, a perovskite material with a relatively high gain coefficient is required. Second, the perovskite material must be very stable under high temperature and intensive light illumination. It is reported that the gain coefficient of $CsPbBr_3$ is around 450 cm^{-1} (the pump intensity is 425 μJ cm^{-2} with a 355 nm nanosecond laser),[8] which is much higher than other conventional semiconductors. In this work, all-inorganic halide perovskite $CsPbBr_3$ nanorods with the optical gain coefficient as high as 954 cm^{-1} were designed and fabricated. Moreover, a microscale hydrophobic zeolite was used to modify perovskites for improved stability.[29] It is interesting to note that the hydrophobic zeolite introduces strong scattering which is beneficial for three-dimensional (3D) random lasing with a quality (Q) factor of 2263. Through the strategy of using lasing instead of luminescence, sensitive humidity sensing was demonstrated. This work provides a new idea for improving the stability of perovskites, which will promote the practical application of perovskite materials and devices.

Results and discussion

Schematic diagrams of the as-grown $CsPbBr_3$ nanorods and modification by a microscale hydrophobic zeolite are shown in Fig. 1a and b. Fig. 1a shows the $CsPbBr_3$ nanorods with tris(diethylamino)phosphine (TDP) ligands on their surface, which have strong steric hindrance that is beneficial for the dispersion of perovskites,[30,31] as shown in the transmission electron microscopy (TEM) image of the $CsPbBr_3$ nanorods in Fig. 1c. And the $CsPbBr_3$ nanorods show a uniform size of about 30 nm length and 10 nm width. The water contact angle of the commercially available SAPO-34 zeolite was measured to be 96° (Fig. S1†),[32–34] implying the hydrophobic properties. As shown in Fig. 1b, the modified perovskite (P-S34) was obtained by adding the hydrophobic zeolite powder into the synthesized $CsPbBr_3$ nanorod solution, and then spin-cast on a quartz substrate after well mixing. The zeolite was uniformly distributed on the substrate with the perovskite coated on it. The surface tension of the hydrophobic zeolite also helps the dispersion of perovskites on its surface, which contributes to the improved performance of the perovskite. Fig. 1d shows the scanning electron microscopy (SEM) image of the hydrophobic zeolite, and its size is about 2 μm. The TEM images of the modified perovskite (P-S34) are shown in Fig. S2,† and it can be clearly seen that the $CsPbBr_3$ nanorods are well-dispersed on the surface of the zeolite. In addition, the SEM images and the digital pictures of the as-grown and P-S34 samples are shown in Fig. S3.† Once again, it can be seen that the composites are

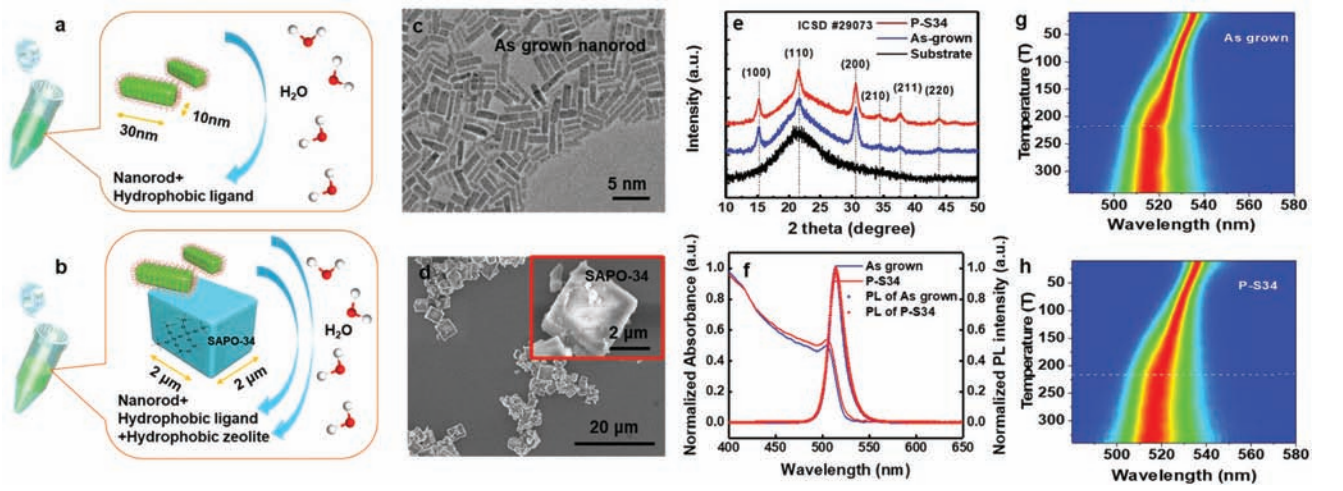

Fig. 1 (a and b) Schematic diagrams of the as-grown $CsPbBr_3$ nanorods and the P-S34 sample. (c) TEM image of the as-grown nanorods. (d) SEM image of the SAPO-34 hydrophobic zeolite. (e) The as-grown and the P-S34 samples of XRD patterns. (f) PL and UV-vis absorption spectra at room temperature. (g and h) Pseudo-color maps of TDPL spectra.

well-dispersed on the surface of the substrate. The X-ray powder diffraction (XRD) patterns of the as-grown and P-S34 samples are shown in Fig. 1e, where the patterns exhibit six distinct sharp peaks located at 15.2°, 21.5°, 30.6°, 34.3°, 37.7°, and 43.9°, respectively. They closely coincide with those of cubic $CsPbBr_3$ obtained from the Inorganic Crystal Structure Database (ICSD 29073), and are assigned to the diffraction of the (100), (110), (200), (210), (211), and (220) planes, respectively (a broad diffraction peak at 21° comes from the quartz substrate).[35,36] It is worth noting that the addition of the hydrophobic zeolite does not change the structure of the nanorod. In addition, the diffraction peaks of the P-S34 sample are sharper than the as-grown ones, implying a better crystal quality. This can be ascribed to the hydrophobic properties offered by the zeolite which give rise to the good dispersion and stability of the perovskite nanorod. Fig. 1f shows the photoluminescence (PL) and UV-vis absorption spectra of the as-grown and the P-S34 samples at room temperature. The peaks of the PL and absorption spectra of these two samples are almost identical (the hydrophobic zeolite has no absorption and emission in the visible range, which is shown in Fig. S4†). The emission peak of the $CsPbBr_3$ nanorod is located at 514 nm, which is consistent with the previously reported $CsPbBr_3$ nanomaterials.[37,38] The narrow line width of PL (~14 nm) and the small Stokes shift (from the absorption peak position to the PL peak position is ~8 nm) indicate the excellent luminous characteristics of the $CsPbBr_3$ nanorod. Fig. 1g and h show pseudo-color maps of temperature-dependent PL spectra of the samples, and the temperature evolution of the emissions from those two samples is almost the same.

In order to study the optical properties of the as-grown and the P-S34 samples in-depth, femtosecond transient absorption (TA) spectroscopy measurement was performed. Optical gain is one of the most important parameters for the optical material and is a key figure-of-merit for lasers, which can be monitored by tracking transient changes in absorption ($\Delta\alpha = \alpha_1 - \alpha_0$) at the band edge after pump excitation, where α_1 is the absorbance after pump excitation and α_0 is the absorbance value of the steady-state absorption spectrum obtained from the UV-vis absorption measurement. The optical gain can be achieved when negative absorption ($\Delta\alpha + \alpha_0 \leq 0$) is observed, namely stimulated emission (SE) surpasses absorption at a given wavelength, and it can be considered to be state filling or population inversion.[8,39,40] For TA spectroscopy, the P-S34 sample was excited by a 355 nm laser with 1 kHz repetition rate and 100 fs pulse width. When the pump fluence exceeds 0.3 μJ cm^{-2}, negative absorption $\Delta\alpha + \alpha_0 \leq 0$ can be observed, which signifies the onset of gain, as clearly depicted in Fig. 2a. It is worth noting that the optical gain appears in the wavelength range of 526–542 nm. To gain more insights, temporal dynamics of the transition of 530 nm in the optical gain region is shown in Fig. 2b, which is in the form of $-\Delta\alpha/\alpha_0$ (namely $\alpha_0 - \alpha_1/\alpha_0$) *versus* time t ($\alpha_0 - \alpha_1/\alpha_0 \geq 1$ is the equivalent of $\Delta\alpha + \alpha_0 \leq 0$, namely the onset of gain). In the first 1.6 ps, $-\Delta\alpha/\alpha_0 < 0$, namely $\Delta\alpha > 0$, is the feature of photo-induced bleaching, which becomes significant with time, and

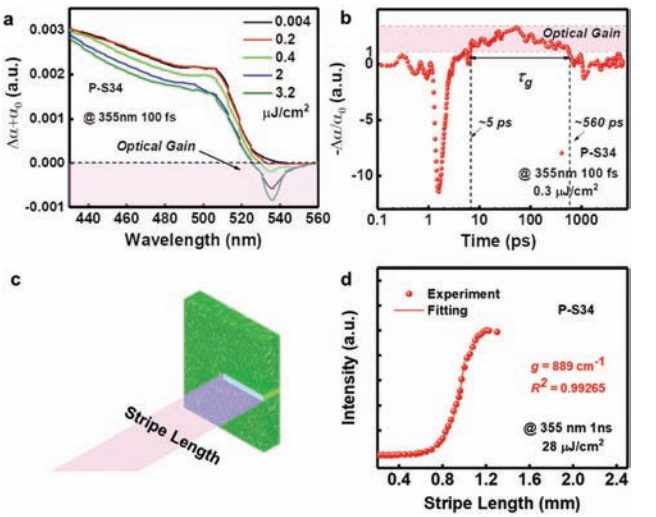

Fig. 2 (a) TA spectra of P-S34 recorded at various pump fluencies. (b) Decay kinetics of P-S34 that is probed at 530 nm with a pump fluence of 0.3 μJ cm^{-2}. (c) Schematic diagram of VLS measurement. (d) Lasing intensity of the P-S34 sample plotted as a function of stripe length.

is probably caused by SE. In 1.6–5.0 ps, $-\Delta\alpha/\alpha_0 \approx 0$, indicating that the electrons of the excited state from photoinduced absorption gradually accumulate. After ~5.0 ps, $-\Delta\alpha/\alpha_0 > 1$, namely $\Delta\alpha < 0$, indicating that the phenomenon of population inversion is gradually appearing.[8,40] In addition, it maintains a value higher than 1 until ~560 ps, which is the time interval of the gain decay lifetimes (τ_g). Obviously, if it has a longer gain decay lifetime, it is advantageous for the ASE of materials. As far as we know, the value of τ_g (~560 ps) in our work is higher than other materials, even other reported perovskite materials.[40]

The value of optical gain can be obtained by the variable stripe length (VSL) measurement, and the schematic diagram is shown in Fig. 2c. The P-S34 sample was excited by a 355 nm pulse laser with 20 Hz repetition rate and 1 ns pulse width. The power density is 28 μJ cm^{-2}, which is equal to about 1.5 times of 0.3 μJ cm^{-2} under femtosecond excitation due to the different repetition rates. In the VSL measurement, the laser was focused to be a stripe through a cylindrical lens (focus length f = 75 mm) and its length is adjusted by the slit. Fig. 2d shows the values of the laser emission intensity of the P-S34 sample with different lengths of the stripe (the laser emission of the P-S34 sample can be found in Fig. 3 and will be described in detail below). The model describing the stripe-length-dependent laser intensity was adopted below:[8,39–41]

$$I = \frac{A(e^{gL} - 1)}{g} \quad (1)$$

where I, g, and L are the laser intensity, the modal gain, and the stripe length, respectively. By fitting the measured data to the model, the modal gain coefficient is then estimated to be ~889 cm^{-1}. The gain coefficient of the as-grown sample is shown in Fig. S5† as 954 cm^{-1}, and this value is among the

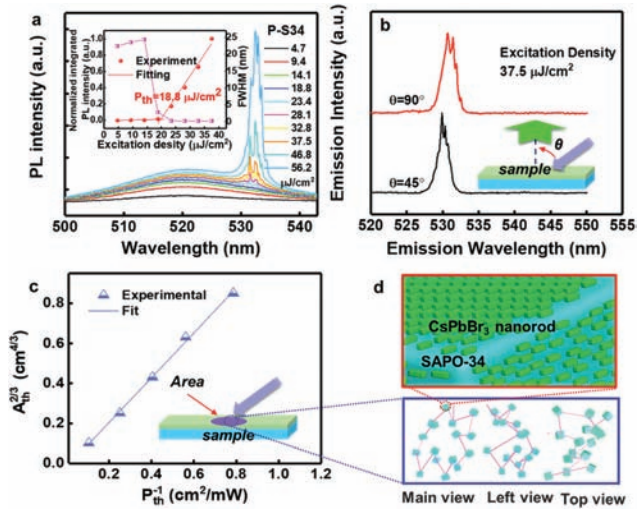

Fig. 3 (a) PL spectra of the P-S34 sample under different pumping densities at room temperature. (b) Emission spectra of P-S34 detected at two different observation angles, and the inset shows the measurement configuration. (c) The random lasing threshold of P-S34 for different excitation areas. (d) Enlarged view of the P-S34 sample and the schematic diagram of quasi-3D random lasing scattering.

largest values obtained for the optical gain of many other materials.

Fig. 3 shows the PL spectra of the P-S34 sample under different pumping densities at room temperature. It can be seen that the sample displays a weak spontaneous emission under low pumping density. When the pumping density exceeds a threshold of ~18.8 μJ cm^{-2}, sharp peaks emerge from the low energy shoulder of the broad spontaneous emission. It shows the phenomenon of amplified spontaneous emission of perovskites, which has been reported.[8,42] When the pumping density further increases, multiple spikes at ~532 nm with line widths of 0.2–0.3 nm can be detected, the intensity of which increases rapidly. The Q factors of lasing modes are in the range of 1773–2660,[40,43] as shown in the inset of Fig. 3a. The PL intensity of these stimulated peaks with respect to pumping density is given in the inset of Fig. 3a. Such a nonlinear increase of the integrated intensity is a characteristic of lasing. It is known that the lasing action requires proper optical feedback. To clarify the lasing mechanism of P-S34, angle-dependent PL measurements were carried out, and the results are plotted in Fig. 3b. It can be clearly seen that different emission spectra can be recorded from different directions, which is qualitatively consistent with the random lasing behavior with coherent feedback.[44–46] In addition, for further verification, the dependence of the excitation area (A_{th}) on the random lasing threshold (P_{th}^{-1}) under constant pump power is presented in Fig. 3c. When the excitation area is increased, the pump threshold needed to create random lasing decreases. Note that the experimental data are consistent with the relationship of $A_{th}^{2/3} \approx KP_{th}^{-1}$, where K is a constant, which is the coherent random laser theory of a 3D random medium.[27,46] It is found that the experimental data can be well-fitted with the formula. Thanks to the strong scattering provided by the hydrophobic zeolites, the lasing mechanism of the P-S34 sample discussed herein can be ascribed to 3D random lasing, as shown in the schematic diagram of Fig. 3d, and for the as-grown sample, only the ASE can be seen, as shown in Fig. S6a and b.†

As discussed above, lasing is much more sensitive to the surrounding environmental situation compared to luminescence. If lasing is used for humidity sensing, good photostability and structural stability of perovskites under high humidity and heat are the most important issues. Fig. 4a shows the integrated intensity of ASE and lasing in ambient environment as a function of the laser shots with 1 ns pulse width at 355 nm, and the inset is the corresponding spectra. The excitation power density was maintained at 28 μJ cm^{-2}, which gives rise to bright emission that can be readily monitored. In the case of the as-grown sample, the ASE intensity firstly increases by about 1 h under continuous pulsed illumination (about 1×10^5 shots) and then decreases. It is because that the surface of perovskite materials can be passivated by O^{2-} in the presence of water and oxygen under illumination, which implies that the as-grown sample is unstable to the environment.[47] And for the P-S34 sample, it is observed that its lasing intensity barely changes over 5 hours (3.6×10^5 shots), implying that the hydrophobic surface tension can maintain the hydrophobicity of perovskites and retain their structural stability. The aging experiment under extreme con-

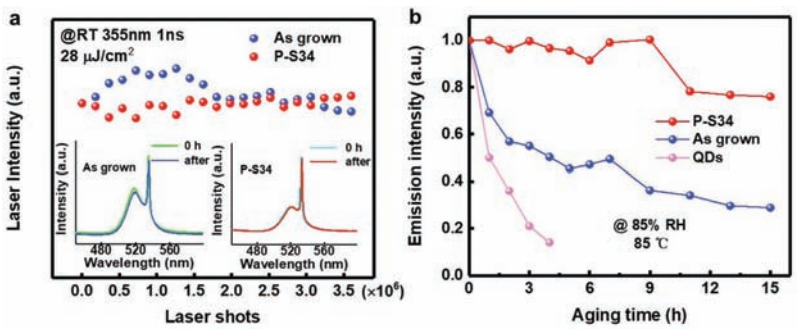

Fig. 4 (a) The lasing intensity of the as-grown sample and P-S34 sample as a function of the number of laser shots under an excitation intensity of 28 μJ cm^{-2}. (b) The emission of the $CsPbBr_3$ QDs, as-grown and P-S34 sample after aging experiment (85% RH at 85 °C) for different times.

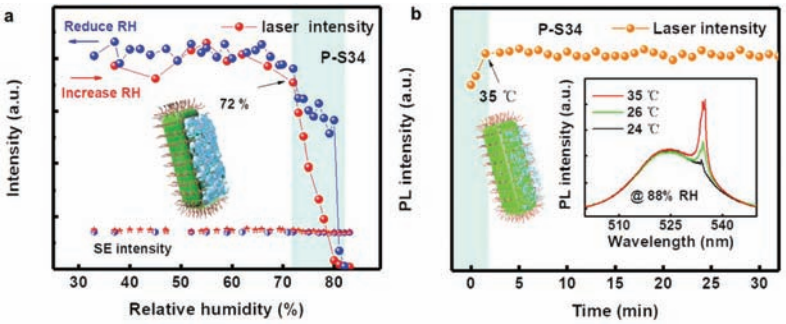

Fig. 5 (a) Lasing and spontaneous emission of the P-S34 sample as a function of RH. (b) The intensity of lasing from the P-S34 sample after being heated to 35 °C at 88% RH as a function of time. The inset is the lasing emission of the P-S34 sample after being heated.

ditions (85% RH at 85 °C) also verified this conclusion, as shown in Fig. 4b. In order to more clearly reflect the stability of the samples discussed herein, traditional perovskite quantum dots (QDs) were used for comparison. These samples were taken out of the aging oven at various time intervals to measure their emission under the excitation of a He–Cd laser with a line of 325 nm. It can be seen in Fig. 4b that the PL intensity of the pristine perovskite QDs drops to 0 after 4 hours. The emission of the as-grown nanorods also decreased to 33% after 15 hours, while the intensity of the P-S34 sample is only slightly reduced. This is consistent with the conclusions drawn from Fig. 4a, which implies that the P-S34 sample exhibits extreme stability at high temperature and high humidity.

In order to measure the changes in the lasing of the modified sample with different humidities, a measurement system with humidity control, humidity monitoring and a PL collection, respectively, is used and is shown in Fig. S7,† of which humidity can be controlled in the range of 25%–98%. As shown in Fig. 5a, the red dots and red stars represent the intensity of lasing and spontaneous emission (SE) as a function of increasing RH for the P-S34 sample, while the blue ones represent the case of reducing RH (they were conducted in the same sample). It is noted that the SE of the P-S34 sample remains the same in the processes of increase and decrease of RH. This is because the hydrophobic surface tension of the modified perovskite prevents the influence of water molecules. This explanation also accounts for the case of lasing under low humidity (30%–72%). However, it is interesting to note that the lasing intensity demonstrates a huge change between 72%–82% RH, with reversible characteristics. It exhibits high sensitivity (the percentage quenching of the humidity sensor was 24%/% RH, which is the part of the initial quenching of the laser to its intensity quenching to 90%).[10] It indicates that the moisture may accumulate as a film of water on the surface of the nanorods when the RH is as high as 72% (inset of Fig. 5a), which leads to the change of the surface refractive index. It is known that lasing is sensitive to the refractive index of the optical path.[45,48] Therefore, the intensity of lasing will decrease with the change of the surface refractive index. However, this water film is unstable, and the moisture will evaporate if the humidity decreases to 30%. Besides, the hydrophobic tension may also contribute to the effect. Thus the intensity of lasing will recover. To verify this phenomenon, a planar heating device was used in this experiment to accelerate the evaporation of moisture, and the spectra are shown in Fig. 5b, where the inset is the schematic diagram of the evaporation of moisture on the surface of nanorods after heating. It can be seen that the lasing intensity is very weak under 88% RH, but its intensity recovered when the P-S34 sample was heated to 35 °C. In addition, the lasing intensity remains the same when the temperature is maintained at 35 °C. Reversible conversion of the laser humidity sensing of the modified sample exposed to 30 and 90% RH is shown in Fig. S8.† It can be seen that the laser intensity remains above 97% after 10 cycles, which indicates good reliability. The SEM and XRD pictures of the P-S34 sample after multiple cycles are shown in Fig. S9.† The insets of Fig. S9a† are the digital pictures of the P-S34 sample without and with ultraviolet light illumination, respectively. It is found that after characterization with multiple cycles, the surface morphology and optical performance of the modified sample are identical, and it can be seen that the P-S34 sample still maintains good quality, which implies the good stability of the material.

Experimental

Materials

Chemicals such as $PbBr_2$, oleic acid (OA), oleylamine (OAm) and hydrobromic acid (HBr, 48%) were purchased from Aldrich, and cesium stearate (Csst), dodecane and tris(diethylamino)phosphine (TDP) were purchased from Aladdin. While indium(III) acetate ($In(OAc)_3$) was purchased from Alfa Aesar, other common reagents, such as ethyl acetate, alcohol, hexane and diethyl ether were purchased from Beijing Chemical Reagent Ltd, China. They were all used without further purification.

Synthesis of $CsPbBr_3$ nanorods

12.5 ml OAm and 8.56 mL HBr solution were mixed in 100 ml ethanol to generate OAmBr. After the reaction solution was

purified and vacuum dried at room temperature, the white OAmBr powder was obtained. 0.0690 g $PbBr_2$ and 0.0652 g OAmBr were mixed in 5 ml dodecane to complete dissolution under 80 °C, and then increased to 180 °C after 0.5 ml OA and 0.5 ml OAm were injected. 0.07828 g Csst and 3 ml dodecane were heated to 140 °C, and then quickly injected into the reaction solution to generate $CsPbBr_3$ crude solution. 0.1458 g In $(OAc)_3$, 1 ml OAm and 9 ml dodecane were mixed and dried under 80 °C for 10 min to generate $In(OAm)_3$. 10 ml $In(OAm)_3$ solution and 6 ml $CsPbBr_3$ crude solution without purification were mixed under flowing nitrogen for 10 min. Then 0.14 ml TDP was injected into the solution and was heated to 50 °C at the rate of 10 °C min^{-1}. After the solution turned colorless, the temperature was further increased to 100 °C. After the reaction solution was purified and centrifuged, the stable $CsPbBr_3$ nanorod solution was obtained, and related growth mechanisms have been published.[30]

Synthesis of zeolite-$CsPbBr_3$ nanorod composites

5 mg hydrophobic zeolite SAPO-34 powder was added into the synthesized $CsPbBr_3$ nanorod solution. The resulting solution was stirred for 10 min to make sure the sample was completely mixed. Afterward, the mixture was spin-cast on the quartz substrate at 2000 revolutions per minute (rpm) for 30 s in air followed by 500 rpm for 5 s. This procedure was repeated 2–3 times to build up the thickness of 100–400 nm of $CsPbBr_3$ nanorod films and 2–3 μm zeolite–$CsPbBr_3$ nanorod layer.

Structure characterization

The crystal structures of the $CsPbBr_3$ nanorods and zeolite–$CsPbBr_3$ nanorod samples (P-S34) were characterized by X-ray powder diffraction (XRD) on a Bruker D8 Discover X-ray diffraction system. Field emission scanning electron microscopy (FESEM) (Hitachi S-4800) was used to measure the microstructures of the SAPO-34 zeolite powder, and transmission electron microscopy (TEM) with an FEI Tecnai G2 F20 microscope operated at 200 kV was used to observe the size and shape of the $CsPbBr_3$ nanorods.

Optical characterization

UV-vis absorption spectra were recorded at room temperature on an ultraviolet and visible spectrophotometer. Steady-state PL spectra were recorded using a Shamrock spectrometer (model no. SR-750-D1-R) and detected using a Newton CCD (model no. DU920P-BU). The temperature dependent PL (TDPL) was obtained using a Horiba iHR550 spectrometer, and the samples were placed in a vacuum chamber and excited at 447 nm working with a 1200 g mm^{-1} grating. The power of the excitation laser is 0.2 mW, and the spot size is ~0.002 cm^2. The temperature was controlled by a closed-cycle helium cryostat at 10–300 K. For TA spectroscopy, pump pulses are at 355 nm (Astrella Ultrafast Ti: Sapphire Amplifier, Coherent, 800 nm, 1 kHz, 100 fs, and the OPerA Solo is Ultrafast Optical Parametric Amplifier, Coherent) and the spot size is ~0.002 cm^2. The samples were excited by a 355 nm pulse laser (CryLas FTSS355-300-STA) at 20 Hz repetition rate and 1 ns pulse width at room temperature for gain measurement (variable stripe length (VSL) measurements) and laser characterization. In the VSL measurement, the excitation beam (power density is 28 μJ cm^{-2}) is focused to be a strip line by a cylindrical lens (focus length f = 75 mm) whose length is controlled by an adjustable slit. The slit width (maximum) is 6 mm and slit width adjustment per revolution is 0.5 mm with a total of 20 scales.

Aging

The samples were placed in an oven that can be kept at a constant temperature and humidity, and the temperature was maintained at 85 °C and 85% RH. The PL of the samples was measured every half hour and a He–Cd laser with a line of 325 nm as the excitation source was used to perform PL measurements. The aging test lasts for 15 hours.

Conclusions

In conclusion, all-inorganic halide perovskite $CsPbBr_3$ nanorods with an optical gain coefficient as high as 954 cm^{-1} were designed and fabricated. Moreover, a microscale hydrophobic zeolite was introduced to modify perovskites for improved stability and the induced strong scattering is beneficial for 3D random lasing with a Q factor of 2263. The photostability and the ageing test under the extreme conditions of high humidity and high temperature (85% RH at 85 °C) indicated that the stability of the P-S34 sample has been significantly improved. Through the strategies of using lasing instead of luminescence, sensitive laser humidity sensing was demonstrated, which exhibits high sensitivity and good reliability. This work provides a new idea of improved stability of perovskites, which will promote the practical application of perovskite materials and devices.

Conflicts of interest

There are no conflicts to declare.

Acknowledgements

This work is supported by the project funded by the China Postdoctoral Science Foundation (2019M661680, 2019M652176), the National Natural Science Foundation of China (11574130, 61674021, 11674038, 61704011, 61904017), the Developing Project of Science and Technology of Jilin Province (20200301052RQ) and the Shenzhen Science and Technology Innovation Commission (Projects No. KQJSCX20170726145748464, JCYJ20180305180553701, and KQTD2015071710313656). Thanks to Shaoqing Chen and Haolin Li for their help with TEM and SEM characterization.

References

1 Y. Liu, Z. Yang and S. Liu, *Adv. Sci.*, 2018, **5**, 1700471.
2 E. H. Jung, N. J. Jeon, E. Y. Park, C. S. Moon, T. J. Shin, T. Y. Yang, J. H. Noh and J. Seo, *Nature*, 2019, **567**, 511–515.
3 A. Kojima, K. Teshima, Y. Shirai and T. Miyasaka, *J. Am. Chem. Soc.*, 2009, **131**, 6050–6051.
4 M. Kim, G. Kim, T. K. Lee, I. W. Choi, H. W. Choi, Y. Jo, Y. J. Yoon, J. W. Kim, J. Lee, D. Huh, H. Lee, S. K. Kwak, J. Y. Kim and D. S. Kim, *Joule*, 2019, **3**, 2179–2192.
5 J. Feng, C. Gong, H. Gao, W. Wen, Y. Gong, X. Jiang, B. Zhang, Y. Wu, Y. Wu, H. Fu, L. Jiang and X. Zhang, *Nat. Electron.*, 2018, **1**, 404–410.
6 S. A. Veldhuis, P. P. Boix, N. Yantara, M. Li, T. C. Sum, N. Mathews and S. G. Mhaisalkar, *Adv. Mater.*, 2016, **28**, 6804–6834.
7 N. Zhang, Y. Fan, K. Wang, Z. Gu, Y. Wang, L. Ge, S. Xiao and Q. Song, *Nat. Commun.*, 2019, **10**, 1770.
8 S. Yakunin, L. Protesescu, F. Krieg, M. I. Bodnarchuk, G. Nedelcu, M. Humer, G. De Luca, M. Fiebig, W. Heiss and M. V. Kovalenko, *Nat. Commun.*, 2015, **6**, 8056.
9 G. Huang, C. Wang, S. Xu, S. Zong, J. Lu, Z. Wang, C. Lu and Y. Cui, *Adv. Mater.*, 2017, **29**, 1700095.
10 W. Xu, F. Li, Z. Cai, Y. Wang, F. Luo and X. Chen, *J. Mater. Chem. C*, 2016, **4**, 9651–9655.
11 M. A. Stoeckel, M. Gobbi, S. Bonacchi, F. Liscio, L. Ferlauto, E. Orgiu and P. Samorì, *Adv. Mater.*, 2017, **29**, 1702469.
12 X. Sheng, Y. Liu, Y. Wang, Y. Li, X. Wang, X. Wang, Z. Dai, J. Bao and X. Xu, *Adv. Mater.*, 2017, **29**, 1700150.
13 J. Chen, Z. H. Mo, X. Yang, H. L. Zhou and Q. Gao, *Chem. Commun.*, 2017, **53**, 6949–6952.
14 Y. Guo and W. Zhao, *Analyst*, 2019, **144**, 388–395.
15 H. S. Jung, P. Verwilst, W. Y. Kim and J. S. Kim, *Chem. Soc. Rev.*, 2016, **45**, 1242–1256.
16 K. Ren, L. Huang, S. Yue, S. Lu, K. Liu, M. Azam, Z. Wang, Z. Wei, S. Qu and Z. Wang, *J. Mater. Chem. C*, 2017, **5**, 2504–2508.
17 W. Yang, J. Xia, G. Zhou, T. Hu, D. Ye, D. Jiang and Q. Li, *Bull. Korean Chem. Soc.*, 2019, **40**, 399–403.
18 S. Yakunin, B. M. Benin, Y. Shynkarenko, O. Nazarenko, M. I. Bodnarchuk, D. N. Dirin, C. Hofer, S. Cattaneo and M. V. Kovalenko, *Nat. Mater.*, 2019, **18**, 846–852.
19 Z. Zhu, Q. Sun, Z. Zhang, J. Dai, G. Xing, S. Li, X. Huang and W. Huang, *J. Mater. Chem. C*, 2018, **6**, 10121–10137.
20 B. Poeggeler, G. Cornélissen, G. Huether, R. Hardeland, R. Józsa, M. Zeman, K. Stebelova, A. Oláh, G. Bubenik, W. Pan, K. Otsuka, O. Schwartzkopff, E. E. Bakken and F. Halberg, *Biomed. Pharmacother.*, 2005, **59**, S220–S224.
21 X. Chen, D. Wang, T. Wang, Z. Yang, X. Zou, P. Wang, W. Luo, Q. Li, L. Liao, W. Hu and Z. Wei, *ACS Appl. Mater. Interfaces*, 2019, **11**, 33188–33193.
22 Y. Liu, H. Lu, J. Niu, H. Zhang, S. Lou, C. Gao, Y. Zhan, X. Zhang, Q. Jin and L. Zheng, *AIP Adv.*, 2018, **8**, 095108.
23 A. D. Wright, C. Verdi, R. L. Milot, G. E. Eperon, M. A. Pérez-Osorio, H. J. Snaith, F. Giustino, M. B. Johnston and L. M. Herz, *Nat. Commun.*, 2016, **7**, 11755.
24 T. C. Wei, S. Mokkapati, T. Y. Li, C. H. Lin, G. R. Lin, C. Jagadish and J. H. He, *Adv. Funct. Mater.*, 2018, **28**, 1707175.
25 A. Loiudice, S. Saris, E. Oveisi, D. T. L. Alexander and R. Buonsanti, *Angew. Chem., Int. Ed.*, 2017, **56**, 10696–10701.
26 L. N. Quan, R. Quintero-Bermudez, O. Voznyy, G. Walters, A. Jain, J. Z. Fan, X. Zheng, Z. Yang and E. H. Sargent, *Adv. Mater.*, 2017, **29**, 1605945.
27 X. Li, Y. Wang, H. Sun and H. Zeng, *Adv. Mater.*, 2017, **29**, 1701185.
28 S. Zou, Y. Liu, J. Li, C. Liu, R. Feng, F. Jiang, Y. Li, J. Song, H. Zeng, M. Hong and X. Chen, *J. Am. Chem. Soc.*, 2017, **139**, 11443–11450.
29 R. Li, Z. Wei, H. Zhao, H. Yu, X. Fang, D. Fang, J. Li, T. He, R. Chen and X. Wang, *Nanoscale*, 2018, **10**, 22766–22774.
30 S. Wang, J. Yu, M. Zhang, D. Chen, C. Li, R. Chen, G. Jia, A. L. Rogach and X. Yang, *Nano Lett.*, 2019, **19**, 6315–6322.
31 T. Xuan, X. Yang, S. Lou, J. Huang, Y. Liu, J. Yu, H. Li, K.-L. Wong, C. Wang and J. Wang, *Nanoscale*, 2017, **9**, 15286–15290.
32 K. Lum, D. Chandler and J. D. Weeks, *J. Phys. Chem. B*, 1999, **103**, 4570–4577.
33 L. Feng, S. Li, Y. Li, H. Li, L. Zhang, J. Zhai, Y. Song, B. Liu, L. Jiang and D. Zhu, *Adv. Mater.*, 2002, **14**, 1857–1860.
34 K. Y. Law and J. Phys, *Chem. Lett.*, 2014, **5**, 686–688.
35 Y. El Ajjouri, F. Palazon, M. Sessolo and H. J. Bolink, *Chem. Mater.*, 2018, **30**, 7423–7427.
36 Q. Van Le, M. Park, W. Sohn, H. W. Jang and S. Y. Kim, *Adv. Electron. Mater.*, 2017, **3**, 1600448.
37 H. Wang, X. Zhang, Q. Wu, F. Cao, D. Yang, Y. Shang, Z. Ning, W. Zhang, W. Zheng, Y. Yan, S. V. Kershaw, L. Zhang, A. L. Rogach and X. Yang, *Nat. Commun.*, 2019, **10**, 665.
38 X. Huang, H. Li, C. Zhang, S. Tan, Z. Chen, L. Chen, Z. Lu, X. Wang and M. Xiao, *Nat. Commun.*, 2019, **10**, 1163.
39 Y. Xu, Q. Chen, C. Zhang, R. Wang, H. Wu, X. Zhang, G. Xing, W. W. Yu, X. Wang, Y. Zhang and M. Xiao, *J. Am. Chem. Soc.*, 2016, **138**, 3761–3768.
40 Y. Wang, M. Zhi, Y. Q. Chang, J. P. Zhang and Y. Chan, *Nano Lett.*, 2018, **18**, 4976–4984.
41 J. Q. Grim, S. Christodoulou, F. Di Stasio, R. Krahne, R. Cingolani, L. Manna and I. Moreels, *Nat. Nanotechnol.*, 2014, **9**, 891.
42 Y. Wang, X. Li, J. Song, L. Xiao, H. Zeng and H. Sun, *Adv. Mater.*, 2015, **27**, 7101–7108.
43 Z. Yang, J. Lu, M. ZhuGe, Y. Cheng, J. Hu, F. Li, S. Qiao, Y. Zhang, G. Hu and Q. Yang, *Adv. Mater.*, 2019, **31**, 1900647.
44 R. Chen, Q. L. Ye, T. He, V. D. Ta, Y. Ying, Y. Y. Tay, T. Wu and H. Sun, *Nano Lett.*, 2013, **13**, 734–739.

45 R. Chen, M. I. Bakti Utama, Z. Peng, B. Peng, Q. Xiong and H. Sun, *Adv. Mater.*, 2011, **23**, 1404–1408.
46 S. F. Yu, C. Yuen, S. P. Lau and H. W. Lee, *Appl. Phys. Lett.*, 2004, **84**, 3244–3246.
47 Y. Wang, Y. Ren, S. Zhang, J. Wu, J. Song, X. Li, J. Xu, C. H. Sow, H. Zeng and H. Sun, *Commun. Phys.*, 2018, **1**, 96.
48 X. Feng, H. Su, Y. Wu, H. Wu, J. Xie, X. Liu, J. Fan, J. Dai and Z. He, *J. Mater. Chem. A*, 2017, **5**, 12048–12053.